Self-propelled swimming of a flexible plunging foil near a solid wall

Bioinspiration & Biomimetics

PAPER

Self-propelled swimming of a flexible plunging foil near a solid wall

Longzhen Dai, Guowei He and Xing Zhang

The State Key Laboratory of Nonlinear Mechanics, Institute of Mechanics, Chinese Academy of Sciences, Beijing 100190, People's Republic of China

E-mail: zhangx@lnm.imech.ac.cn

Abstract

Numerical simulations are conducted to investigate the influences of a solid wall on the self-propelled swimming of a flexible plunging foil. It is found that the presence of a solid wall enhances the cruising speed, with the cost of increasing input power. Rigid foil can achieve high percentage increase in cruising speed when swimming near a solid wall, but the propulsive efficiency may be reduced. Foils with some flexibility can enjoy the enhancements in both cruising speed and propulsive efficiency. Another advantage of the flexible foils in near-wall swimming is that smaller averaged lateral forces are produced. The effects of wall confinement on the wake structure and the vortex dynamics are also studied in this paper. The results obtained in this study shed some light on the unsteady wall effect experienced by aquatic animals and also inform the design of bio-mimetic underwater vehicles which are capable of exploiting the wall effect.

1. Introduction

Boundary confinements are frequently encountered in the world of swimmers and flyers. It is well known that the presence of a boundary can affect their locomotion. Thus for making predictions or understanding flow physics, it is crucial to account for the effect of boundary confinement in theoretical models.

In the studies of macro-scale biolocomotion, the effect of boundary confinement is also termed as ground effect, or wall effect. Such effect can be found in steady gliding with fixed-wing configuration. For example, gliding black skimmer (*rhyncops nigra*) can exploit ground effect to increase its forage efficiency [1]. Gliding pelican was found to achieve significant energy savings from ground effect [2]. Similar aerodynamics advantage was found in flying fish when gliding close to the sea surface [3]. Ground effect is also observed in undulatory swimming with deforming body or fin. For example, steelhead trout was found to alter its kinematics under the influence of channel side walls. The wall effect reduced its tail-beat amplitude and swimming speed, while the tail-beat frequency was not affected [4]. The kinematics of plaice (which is a typical example of benthic fish) were also affected by the presence of a substrate [5]. The plaice's tail-beat amplitude reduced when swimming near the ground.

Its tail-beat frequency increased with speed when swimming near the bottom, but was independent of speed when swimming away from the bottom.

Although the ground effects in steady gliding and undulatory swimming seem to be alike, the physical mechanisms behind them are actually very different. In the case of steady gliding, ground effect improves the aerodynamic performance by increasing the lift-to-drag ratio. The increase in lift-to-drag ratio is the consequence of (a) enhanced lift production due to the high pressure between the lifting surface and the boundary, and (b) lower induced drag due to the inhibition of wing-tip vortices. Mathematical models based on traditional steady aerodynamics theory have been used to predict the gliding performance of birds near the ground or the sea surface [6, 7]. In the case of undulatory swimming near a surface, the wall effect becomes unsteady due to the time-varying pressure and flow structures in between the swimmer and the surface. Unlike the steady wall effect, the unsteady wall effect in undulatory swimmers is still not fully understood. As a first step towards understanding the unsteady wall effect experienced by aquatic animals, the influences of an underneath boundary on the propulsive performance of mechanical locomotors have been investigated.

Analytical approach was first used by Tanida [8] to study the fluttering of a soft plate in oscillating mode near a channel wall. The results showed that the wall effect can increase the thrust and propulsive efficiency. Iosilevskii [9] used asymptotics to predict the unsteady lift and drag on a two-dimensional, oscillating airfoil near a flat surface.

Recently, experiments were carried out by Quinn *et al* [10] to study rigid airfoils undergoing pitching oscillations near a solid surface, and it was demonstrated that thrust can be enhanced by the wall effect while the propulsive efficiency remained a constant. In another experiment conducted by Quinn *et al* [11], a flexible rectangular panel was actuated at the leading edge near the wall of a water channel. For a given actuation mode under the self-propelled condition, it was found that the panel swam faster near the channel wall while maintaining the same propulsive economy. Under the tethered condition, it was found that the panel produced more thrust near the channel wall. In the work by Fernandez-Prats *et al* [12], the propulsive dynamics of a flexible undulating foil under self-propelled condition near a wall was investigated. In the experiments on stingray-inspired flexible fins [13], it was found that under most kinematic conditions, the robotic fins cannot swim faster near a solid wall, while the cost of transport can increase by up to 10%.

A few numerical studies on the unsteady wall effect can also be found in the literature. Quinn *et al* [10] used the unsteady potential flow method to compute thrust and lift on a pitching aerofoil close to a solid boundary. Liang *et al* [14] employed a potential-flow-based discrete vortex method to investigate the unsteady wall effect in heaving airfoils. Viscous flow simulations have been conducted to study the aerodynamic behavior of an inverted airfoil (based on Formula One car front wing) which oscillated near the ground [15, 16]. The two works above focused on the wall effect on the production of down force (negative lift force).

As seen from the literature review above, the unsteady wall effect is a relatively new research topic in biolocomotion. Whether the presence of an underneath wall enhances the propulsive performance is still inconclusive. Motivated by the desire to achieve a better understanding of the unsteady wall effect, in the current work, we conduct simulations on the self-propulsion of a flexible plunging foil near a solid boundary. To the best of our knowledge, numerical studies which solve the Navier–Stokes equations to quantify the wall effect on the propulsive performance of free-swimming flapping foils still lack in the literature. Two main questions are considered this study: are there any energetic benefits by swimming near a solid wall, and how does the presence of a boundary modify the wake structure behind the swimmer?

The rest of the paper is arranged as follows. Section 2 presents the model problem, numerical methodology and simulation set-ups. Section 3 presents the results and discussions, including the effects
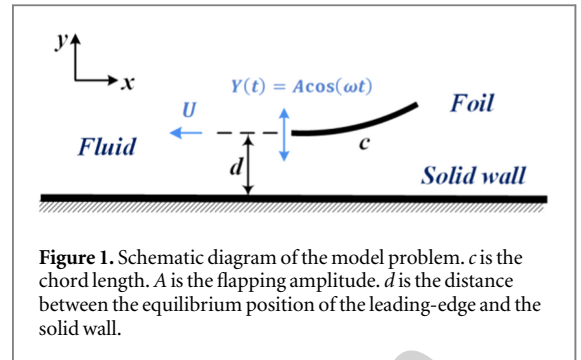
Figure 1. Schematic diagram of the model problem. *c* is the chord length. *A* is the flapping amplitude. *d* is the distance between the equilibrium position of the leading-edge and the solid wall.

of an underneath wall on the propulsive performance, the production of averaged lift and the wake structure. Finally, some conclusions are drawn in section 4.

2. Model problem and numerical methodology

2.1. Model problem and governing equations

We consider the self-propulsion of a flexible plunging foil near a solid wall. The fluid flow around the foil is assumed to be incompressible and laminar. Here the foil is simplified as an inextensible filament which is actuated by a prescribed vertical motion at its leading edge. In the horizontal direction, no constraint is imposed and the foil is allowed to move freely.

In this paper, the plunging motion is prescribed as $Y(t) = A\cos(\omega t)$, where Y is the vertical position of the leading-edge, A and ω are the plunging amplitude and the circular frequency, respectively. Figure 1 is a schematic diagram of the model problem considered in this study. Here c is the chord length of the foil; d is the vertical distance between the equilibrium position of the leading edge and the solid wall. The dimensionless plunging amplitude and dimensionless wall distance are defined as $\bar{A} = A/c$ and $\bar{D} = d/c$, respectively.

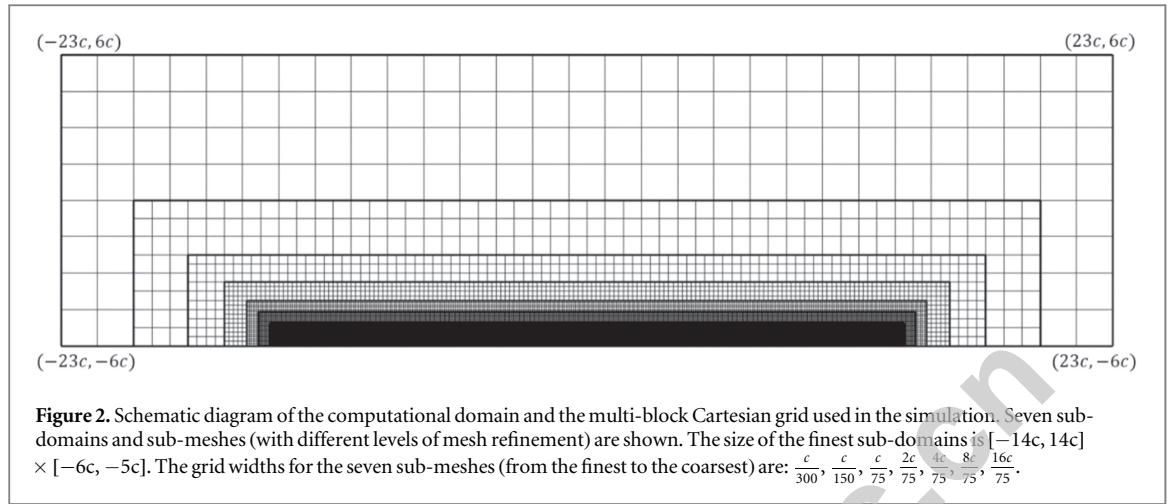The fluid flow is governed by the incompressible Navier–Stokes equations written in a dimensionless form as:

$$\frac{\partial \boldsymbol{u}}{\partial t} + \nabla \cdot (\boldsymbol{u}\boldsymbol{u}) = -\nabla p + \frac{1}{Re_p}\nabla^2\boldsymbol{u} + \boldsymbol{f}, \quad (1)$$

$$\nabla \cdot \boldsymbol{u} = 0. \quad (2)$$

Here $\boldsymbol{u}$ is the velocity and p is the pressure. $\boldsymbol{f}$ is the dimensionless Eulerian forcing term which mimics the effect of the immersed foil on the fluid flow.

All quantities in equations (1) and (2) are scaled by the reference length c and reference time c/U_{ref}, where the reference velocity U_{ref} is defined as the maximum plunging velocity, $A\omega$, of the leading edge. Re_p is the plunging Reynolds number which is defined as $\rho_f U_{ref} c/\mu$, where ρ_f, μ are the density and dynamic viscosity of the fluid, respectively.

The motion of the flexible foil is governed by the structure equations written in a dimensionless form as:

Figure 2. Schematic diagram of the computational domain and the multi-block Cartesian grid used in the simulation. Seven sub-domains and sub-meshes (with different levels of mesh refinement) are shown. The size of the finest sub-domains is $[-14c, 14c] \times [-6c, -5c]$. The grid widths for the seven sub-meshes (from the finest to the coarsest) are: $\frac{c}{300}, \frac{c}{150}, \frac{c}{75}, \frac{2c}{75}, \frac{4c}{75}, \frac{8c}{75}, \frac{16c}{75}$.

$$\beta\frac{\partial^2 \mathbf{X}}{\partial t^2} - \frac{\partial}{\partial}\left(\xi\frac{\partial \mathbf{X}}{\partial s}\right) + \frac{\partial^2}{\partial s^2}\left(\gamma\frac{\partial^2 \mathbf{X}}{\partial s^2}\right) = -\mathbf{F}, \quad (3)$$

$$\frac{\partial \mathbf{X}}{\partial s} \cdot \frac{\partial \mathbf{X}}{\partial s} = 1. \quad (4)$$

Here $\mathbf{X}$ is the position vector; s is the dimensionless Lagrangian coordinate along the arc length; $\mathbf{F}$ is the dimensionless Lagrangian forcing term which accounts for the interaction between the foil and the fluid.

The dimensionless equations (3) and (4) are also obtained by scaling space and time with c and c/U_{ref}, respectively. β, ξ, γ are the density ratio of the foil to the fluid, the dimensionless tension coefficient and the dimensionless bending rigidity, respectively. The definitions of these three parameters are:

$$\beta = \frac{\rho_s}{\rho_f c}, \xi = \frac{T}{\rho_f U_{\text{ref}}^2 c}, \gamma = \frac{B}{\rho_f U_{\text{ref}}^2 c^3}, \quad (5)$$

where ρ_s is the *linear* density of the flexible foil. T and B are the dimensional tension and bending rigidity, respectively.

2.2. Numerical methodology

To numerically simulate the model problem, a loosely-coupled fluid–structure interaction (FSI) solver is used. In the FSI solver, the fluid flow and foil's movement are sequentially advanced by one step in time. In the fluid part, the incompressible Navier–Stokes equations are solved by using the direct-forcing immersed boundary method based on the discrete stream function formulation [17]. In the structural part, the inextensibility condition (4) is satisfied by solving a Poisson equation for the dimensionless tension ξ. The governing equation (3), together with the Poisson equation for ξ, are solved by using a finite difference method based on staggered grids [18]. The FSI solver used in this study has been extensively validated in [19].

2.3. Simulation set-ups

In this work, numerical simulations are performed on a rectangular domain of $[-23c, 23c] \times [-6c, 6c]$. The

solid wall is represented by the bottom side of the computational domain.

A multi-block Cartesian mesh with hanging-nodes [17] is used in this study. Comparing with the single-block stretched mesh, this locally-refined mesh can drastically reduce the total number of mesh points needed for achieving the comparable resolution. A schematic diagram of the multi-block Cartesian mesh is shown in figure 2. In this study, we use a mesh which consists of seven blocks with different resolutions to conduct the simulations. The finest sub-mesh, which is generated on the sub-domain encompassing the flapper, has 301 grid points along the chord length. The sub-meshes generated on other sub-domains are coarsened level-by-level toward the outer boundary by doubling the grid width. The total number of grid points for the multi-block mesh is approximately 3 million.

The non-slip boundary condition is imposed on the front, bottom and rear sides of the computational domain, while the free-slip boundary condition is imposed on top side. The non-slip boundary condition on the flexible foil is realized by using the direct-forcing immersed boundary method proposed in [17]. For the structure solver, the leading edge is treated as a clamped end without horizontal constraints, while the trailing edge is treated as a free-end [19].

Initially, the foil is parallel to the solid wall with its leading edge being placed at $(12c, -6c + d + \text{A})$. The initial velocity of the fluid is set to zero. The time steps for the simulations are chosen such that the maximum CFL number based on the maximum velocity magnitude is 0.5.

3. Results and discussion

3.1. Control parameters

The physical parameters used in the simulations are listed in table 1. For all simulations, the density ratio, the dimensionless flapping amplitude and the flapping Reynolds number are set to 0.03, 0.1 and 200,

Table 1. Physical parameters used in the simulations.

Re_p	200
$\bar{A}$	0.1
β	0.03
γ	1.0, 3.0, 10.0, 30.0, ∞
$\bar{D}$	0.2, 0.22, 0.25, 0.3, 0.35, 0.4, 0.5, 0.7, 1.2, 2.2, 6.0

respectively. The density ratio and dimensionless amplitude are comparable with those in some experimental studies [13]. As a first step towards unveiling the physical mechanism in unsteady wall effect, we use a Reynolds number which is smaller by two orders in magnitude than those of the mechanical flappers [11, 13] or the living stingrays [20]. The use of a reduced Reynolds number is based on the facts that (a) the flow physics in flapping-foil systems is relatively insensitive to the Reynolds number (at least in the range of $10^2 < Re < 10^4$), and (b) a smaller Reynolds number makes the simulations more tractable.

Before investigating into the wall effect, we first consider the case with negligible wall effect ($\bar{D} = 6.0$). We compute three key parameters for assessing the propulsive performance, i.e., the cruising speed U_c, the input power P_s, and the propulsive efficiency η [19]. The cruising speed is the time-averaged horizontal velocity achieved by the leading edge. The input power is the time-averaged power required to produce the oscillation and the forward motion of the foil. The propulsive efficiency is the ratio of the foil's kinetic energy to the input work within one flapping period. Mathematically, the definitions of the three parameters are:

$$\begin{cases} U_c = -\dfrac{1}{T_p}\int_0^{T_p}\left(\dfrac{\partial X}{\partial t}\right)_{s=1}\mathrm{d}t, \\[2mm] P_s = \dfrac{1}{T_p}\int_0^{T_p}\int_0^1\left(\boldsymbol{F}\cdot\dfrac{\partial \boldsymbol{X}}{\partial t}\right)\mathrm{d}s\,\mathrm{d}t, \\[2mm] \eta = \dfrac{\frac{1}{2}\beta U_c^2}{T_p P_s}, \end{cases} \quad (6)$$

where T_p is the dimensionless flapping period. These three parameters are evaluated after the periodically steady state is reached.

The variations of cruising velocity and efficiency with increasing bending rigidity are shown in figure 3. In this work, five representative bending rigidities, namely, 1.0, 3.0, 10.0, 30.0 and ∞, are selected to study the wall effect. $\gamma = 3.0$ and $\gamma = 10.0$ represent the bending rigidities for achieving the optimal efficiency and optimal cruising speed, respectively. $\gamma = 1.0$ and $\gamma = 30.0$ are two suboptimal bending rigidities, in terms of the cruising speed and efficiency achieved. In addition to these four bending rigidities, the rigid limit of a flexible flapper ($\gamma = \infty$) is also considered. For this case, the FSI simulation is conducted by coupling the equations for the fluid motion and the Newton's second law which governs the horizontal

motion of a *rigid* foil [19] (eqautions (3) and (4) are not used). For reference purpose, the values for the cruising speed, input power and propulsive efficiency at these five bending rigidities are listed in table 2.

To study the influence of wall effect on performance, cases with different wall proximities in the range of $0.20 \leqslant \bar{D} \leqslant 6.0$ are simulated, for the five bending rigidities selected. Note that $\bar{D} = 0.20$ is the closest wall proximity considered in this work. We do not consider even smaller $\bar{D}$ for the following two reasons. First, the lack of mesh resolution prevents us from accurately predicting the flow in the narrow clearance. Second, for foils with moderate or high flexibilities, the trailing edges may even collide with the wall and such collision further complicates the problem.
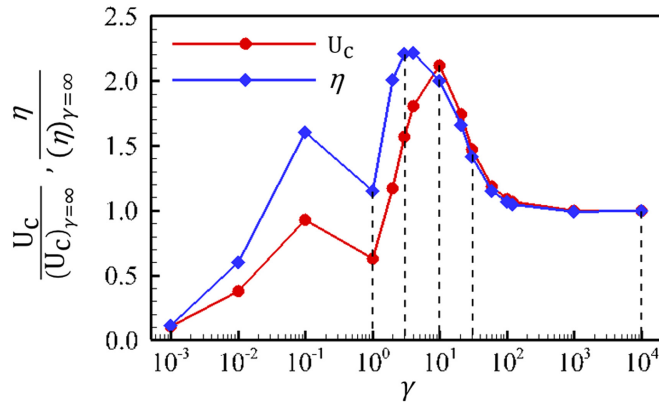
3.2. Mesh sensitivity test

To ensure that the solutions obtained are independent of the mesh width and domain size, a sensitivity test is conducted for the case of $\gamma = 3.0$ and $\bar{D} = 0.20$. In this case, the narrowest possible gap between the flapper and underneath wall is formed due to the highest trailing-edge amplitude and the closest wall proximity. To resolve the flow in the small gap, a very dense mesh is required. This case is thus the most stringent one for the mesh sensitivity test.

Three meshes with different resolutions are generated for the sensitivity test. The detailed information for the meshes used in the test are summarized in table 3. The time histories of the leading-edge's horizontal velocity and the vorticity at one mark point, obtained by using these three meshes, are shown in figure 4. Mesh convergence behaviors are clearly seen from the solutions on the medium and fine meshes. In addition, we also test the sensitivity of the solution to the domain size by using a larger computational domain of $[-28c, 28c] \times [-6c, 9c]$. Another mesh with the resolution comparable to that of the medium mesh is generated on the enlarged domain. It turns out that the solution obtained is barely affected by the using of the enlarged domain. Thus, we are confident that the artifacts caused by the far field boundaries (such as unphysical blocking and shear stresses on the flow) are insignificant. To summarize, convergent and mesh-independent solutions can be obtained by using the medium mesh on a computational domain of $[-23c, 23c] \times [-6c, 6c]$.

3.3. Wall effect on propulsive performance

The influences of wall proximity on the propulsive performance of the flappers with various bending rigidities are summarized in figure 5.

It is clearly seen that the wall effect becomes less obvious for $\bar{D} \geqslant 2.2$. In the range of $0.2 \leqslant \bar{D} < 2.2$, for almost all bending rigidities considered here, the cruising velocity and the input power increase monotonically with decreasing $\bar{D}$. The only exception is the

Figure 3. Variations of cruising velocity and efficiency with increasing bending rigidity for the case of negligible wall effect ($\bar{D} = 6.0$). The cruising velocity and efficiency in this plot are normalized by the corresponding values obtained at the rigid limit ($\gamma = \infty$). For plotting the entire curve within a limited range of γ, the rigid limit is replaced by an extremely large value of 10^4.

Table 2. Cruising speed, input power and propulsive efficiency achieved at $\bar{D} = 6.0$, for the five bending rigidities selected.

γ	$(U_c)_{\bar{D}=6.0}$	$(P_s)_{\bar{D}=6.0}$	$(\eta)_{\bar{D}=6.0}$
1.0	0.8994	0.6946	0.0278
3.0	2.1989	2.2699	0.0509
10.0	2.9442	4.5358	0.0456
30.0	2.0671	3.1308	0.0326
∞	1.3976	2.0541	0.0227

Table 3. Information for the meshes used in the mesh sensitivity test.

Mesh	Points/chord length (finest sub-mesh)	Total grid points (M)	Total levels of refinement
C	201	1.6	6
M	301	2.8	7
F	401	5.4	7
M^L	301	3.1	7

Note. C: coarse mesh; M: medium mesh; F: fine mesh; M^L: mesh of medium resolution on an enlarged domain.

input power for $\gamma = 3.0$, which almost remains unaltered in the presence of a solid wall. It is also seen that foils with very low or very high bending rigidities ($\gamma = 1$, 30 and ∞) tend to gain a high *percentage* of velocity increase, while the velocity benefits in foils with moderate flexibilities ($\gamma = 3$ and 10) are much less. Very rigid foils ($\gamma = 30$ and ∞) in wall effect tend to suffer from a high percentage increase in input power. For very soft foil and foils with moderated bending righties ($\gamma = 1$, 3 and 10), the relative increases in input power are much lower. Among all cases considered in this study, the highest percentage increases in cruising velocity and input power are 66% and 149%, respectively.
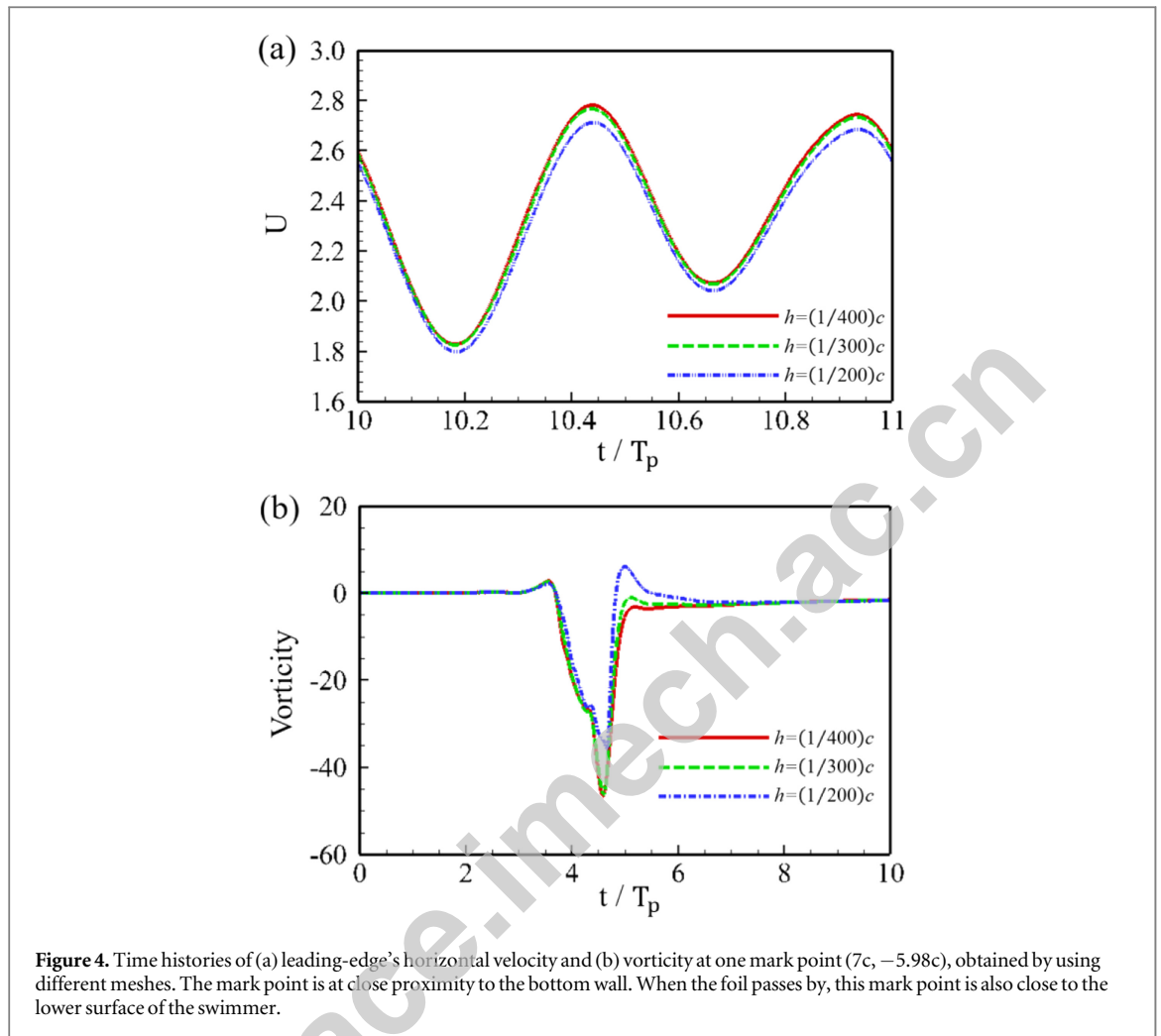
The trends of propulsive efficiencies with decreasing $\bar{D}$ are more complicated. For $\gamma = 3$, 10 and 30, the efficiencies increase monotonically with decreasing $\bar{D}$, while this monotonicity is not seen in the efficiencies of the most flexible and the rigid foils. The highest percentage increase in efficiency (35%) is gained by the most flexible foil at $\bar{D} = 0.2$. In a certain range of $\bar{D}$, the most flexible and the rigid foils may suffer from a reduction in efficiency. The largest percentage reduction in efficiency (14%) is found in the rigid foil at $\bar{D} = 0.5$.

Here we compare the observations of this work with those from some recent studies. The finding that wall effect can enhance cruising speed is in consistency with the results from Quinn *et al* [11] and Fernandez-Prats *et al* [12], where free-swimming experiments were conducted on flexible pitching (or plunging) foils near a solid boundary. However, the current finding is in contrast with that from Blevins and Lauder [13], where almost no gain in the cruising speed was found in a stingray-inspired robotic model swimming near the substrate. As to the propulsive efficiency, it seems that inconsistency exists between our finding and that of Quinn *et al* [11], where the propulsive *economy* was found to be unaffected by the presence of a solid boundary. However, this inconsistency could be caused by the different metrics used to quantify the efficiency. The propulsive economy defined in Quinn *et al* [11] is a dimensional quantity which represents the 'distance traveled per energy input to the fluid', and is not equivalent to the propulsive efficiency defined in equation (6).

3.4. Wall effect on production of averaged lift

Under the self-propelled condition, the averaged streamwise force is always zero. Since the up-down symmetry of the flow field is broken by the introduction of the underneath wall, the foil may experience a nonzero averaged lateral (or lift) force. The time-averaged lift force is computed by
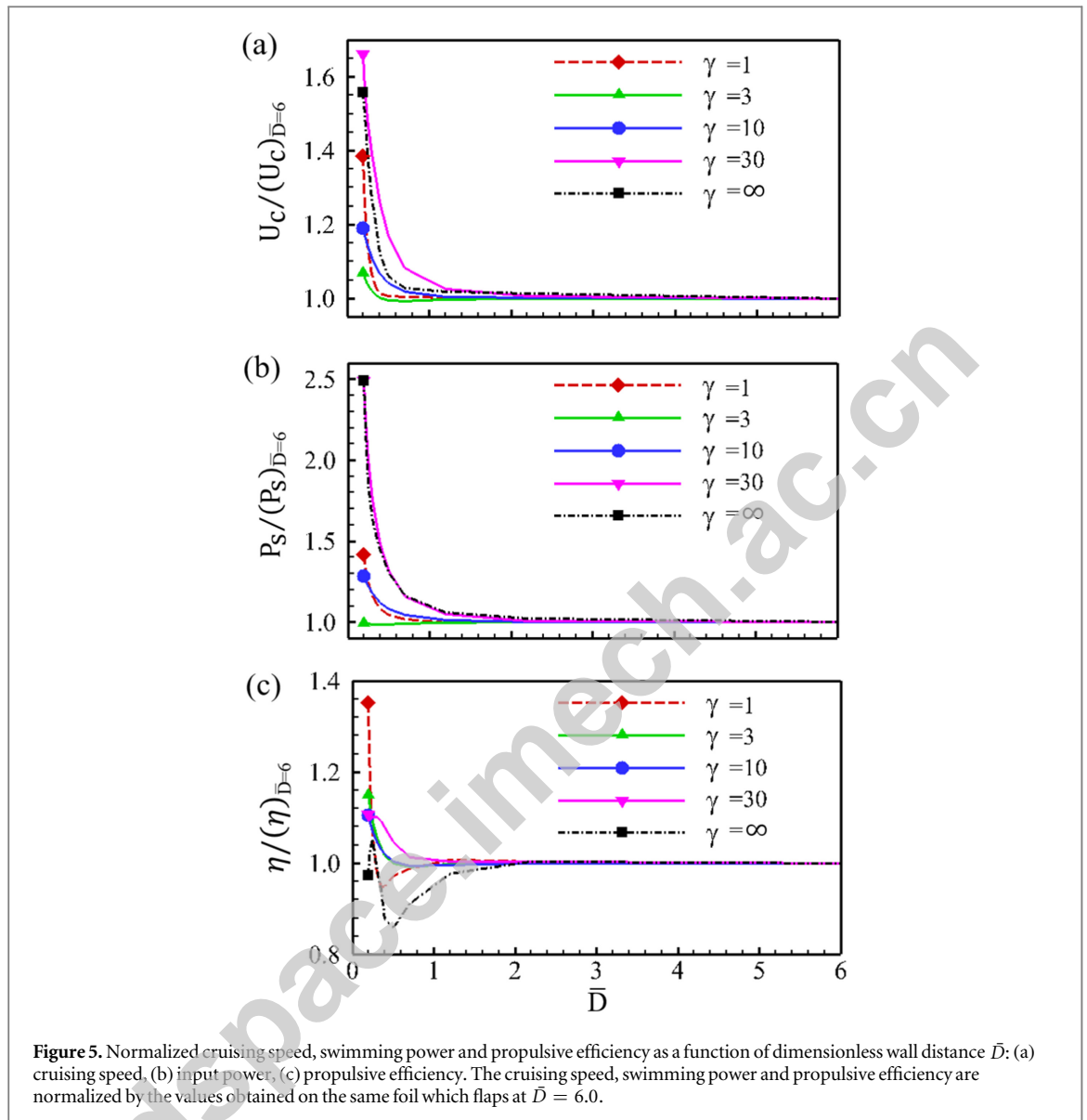
Figure 4. Time histories of (a) leading-edge's horizontal velocity and (b) vorticity at one mark point (7c, −5.98c), obtained by using different meshes. The mark point is at close proximity to the bottom wall. When the foil passes by, this mark point is also close to the lower surface of the swimmer.

$$\bar{F}_y = \frac{1}{T_p} \int_0^{T_p} \left(\int_0^1 F_y \, ds \right) dt. \tag{7}$$

Figure 6 shows the normalized averaged lift forces as a function of $\bar{D}$, for flappers with various bending rigidities. It is seen that the wall effect on the averaged lift forces becomes less obvious for $\bar{D} \geqslant 2.2$. It is also noticed that the averaged lift forces do not approach zero with increasing $\bar{D}$. The offset from zero at $\bar{D} = 6.0$ (which is positive for $\gamma = \infty$ and negative for other bending rigidities) is caused by the asymmetry in the boundary conditions (free-slip on the top and no-slip at the bottom). Since the offset from zero is very small in magnitude (which never exceeds 2% of the root-mean-square (rms) lift), this numerical artifact has barely any influences on the study of the wall effect.

In the range of $0.2 \leqslant \bar{D} < 2.2$, the trends of averaged lift forces with decreasing $\bar{D}$ are very complicated. For $\gamma = 1$ and $\gamma = 30$, the averaged lift forces are always negative, which indicates that the foils always experience an attraction towards the wall. The largest magnitude of the negative lift force, which is approximately 16% of the rms lift force at $\bar{D} = 6.0$, is achieved at $\bar{D} = 0.2$ in the foil of $\gamma = 30$. For the other three bending rigidities (3, 10 and ∞), the

averaged lift forces can be either negative or positive, depending on the values of $\bar{D}$. A positive averaged lift force indicates that the foils experience a repulsion from the wall. The largest magnitude of the positive lift force, which is approximately is 20% of the rms lift force at $\bar{D} = 6.0$, is achieved at $\bar{D} = 0.2$ in the rigid foil. The averaged lift forces experienced by the foils of $\gamma = 3$ and $\gamma = 10$ are actually quite small, with the largest magnitude being less than 10% of the rms lift at $\bar{D} = 6.0$. For $\gamma = 3$, 10 and ∞, an equilibrium point (where the averaged lift is zero) can be found in the range of $0.35 < \bar{D} < 0.7$. These equilibrium points can be categorized as *stable* equilibrium point, in the sense that if the foil is free to move laterally, it will always return to the equilibrium position after small disturbances.

Here the trends of averaged lift forces with varying wall distance reported in this study are also compared with those from some recent works. The trend of the averaged lift force in the rigid foil ($\gamma = \infty$) is found to be consistent with that reported in [10], where *inviscid* simulations were conducted to study the wall effect on a *rigid* pitching foil. This suggests that the production of averaged lift is only marginally affected by the inclusion of fluid viscosity. In another recent experimental

Figure 5. Normalized cruising speed, swimming power and propulsive efficiency as a function of dimensionless wall distance $\bar{D}$: (a) cruising speed, (b) input power, (c) propulsive efficiency. The cruising speed, swimming power and propulsive efficiency are normalized by the values obtained on the same foil which flaps at $\bar{D} = 6.0$.

study on flexible plunging foils near a surface [11], no averaged lateral (lift) forces were detected. We conjecture that the flexible foils in [11] may still experience some non-zero averaged lift forces. However, due to the range of bending rigidity considered in that study, these forces were too small and hard to measure.
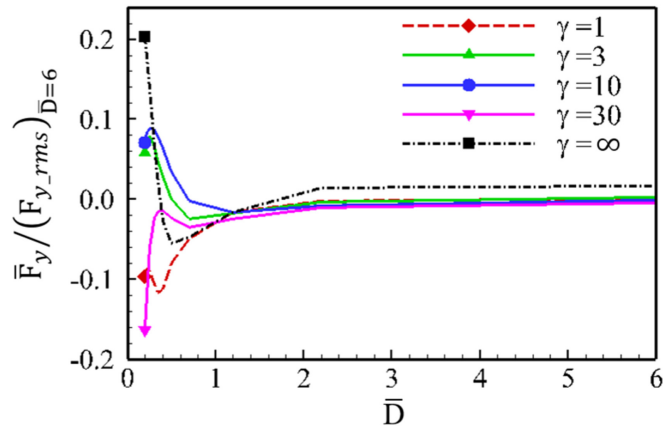
3.5. Wall effect on wake symmetry and vortex dynamics

The wake structures for various wall proximities and bending rigidities are shown in figure 7. From this figure, it is seen that when the free-swimming occurs away from the wall ($\bar{D} = 6.0$), a reversed Karman vortex street is the wake structure which emerges behind the foil. In the reversed Karman vortex street, the vortex cores are evenly spaced and arranged in a staggered fashion. This wake structure is symmetric with respect to the horizontal line corresponding to the equilibrium position of the leading-edge. Since

two single vortices with opposite signs are shed into the wake during one flapping cycle, this pattern of vortex formation is often termed as '2 S' mode. Among the vortex streets for the foils with three different bending rigidities, the largest spacing between two neighboring vortices is found in the foil with moderate flexibility. The reason behind this phenomenon is that the foil with moderate flexibility achieves the highest cruising speed.

The introduction of an underneath wall breaks the symmetry of the wake structure. Under the influence of the wall effect, the positive and negative vortex cores now appear in pairs (dipoles). Due to the ascending motion of these dipoles, the vortex streets now become up-tilted. During ascending, the dipoles also undergo an anticlockwise spinning motion. With deceasing wall distance, the vortex dipoles become more compact, the deflection angle of the vortex street becomes larger, and the spinning motion of the dipoles also becomes more noticeable. Although some
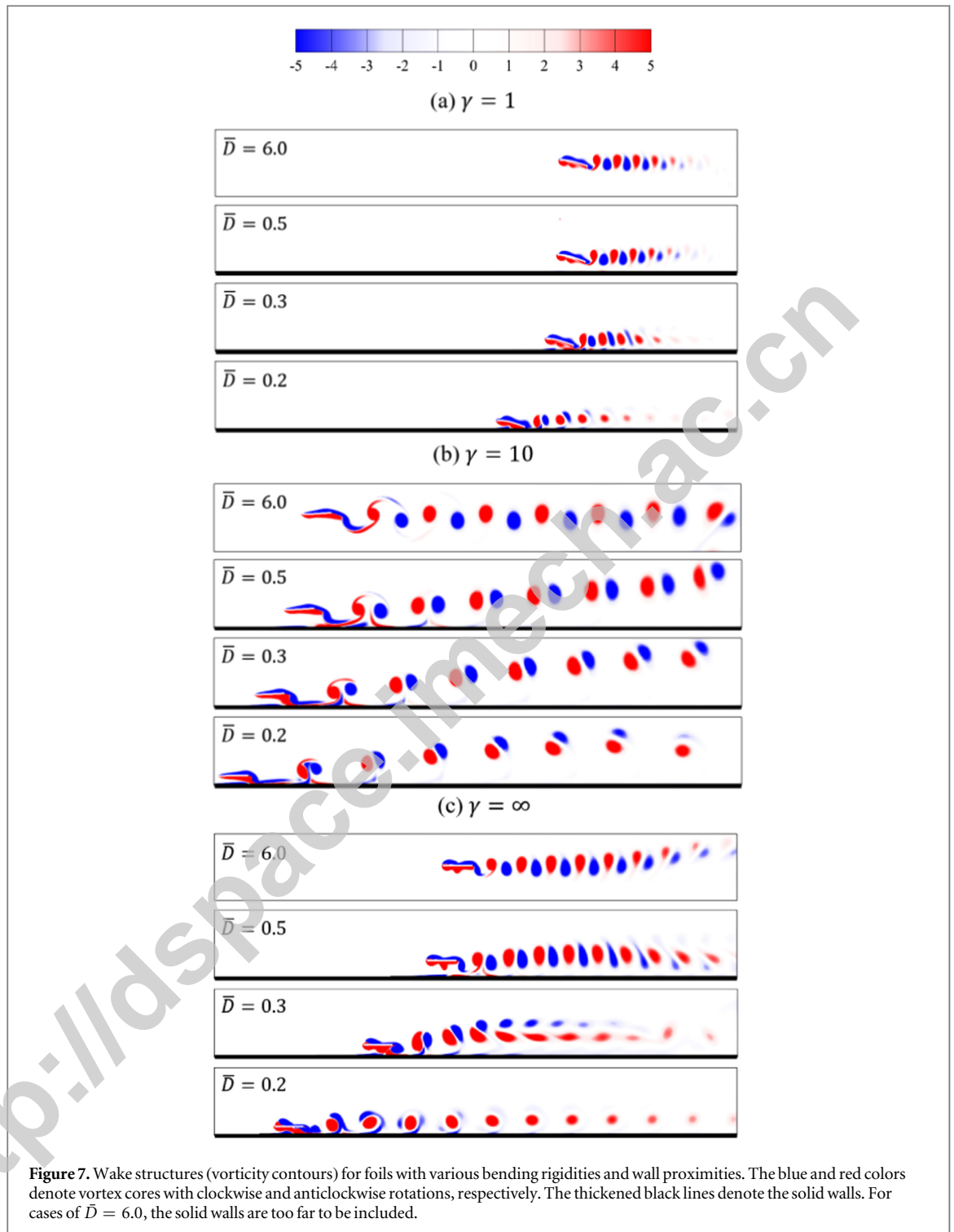
Figure 6. Normalized time-averaged lift forces as a function of wall proximity. The time-averaged lift forces are normalized by the rms lift forces obtained at $\bar{D} = 6.0$. The reference values used in the normalization are 2.124, 6.254, 13.445, 14.020 and 13.196, for $\gamma = 1$, 3, 10, 30 and ∞, respectively.

common features exist in the wall effects for foils with different bending rigidities, some differences can still be found. For foil with moderate flexibility ($\gamma = 10$), the deflected vortex street consisting of dipoles can extend to the far wake. For the most flexible foil ($\gamma = 1.0$), however, the vortex strength becomes lower and the vortex street also decays more rapidly. For the rigid foil ($\gamma = \infty$), the dipoles are highly distorted in the far wake due to the fact that the negative vortices become too weak. Under extreme wall effect ($\bar{D} = 0.2$), the negative vortices almost completely disappear and only one row of positive vortices is left in the far wake.

For a better understanding of the physical mechanisms behind the wall effects on vortex dynamics, a close view of the near wake structures at five different phases during one flapping cycle for the foil with moderate bending rigidity and moderate wall effect ($\gamma = 10.0$ and $\bar{D} = 0.3$) is shown in figure 8. A schematic explanation of the mechanisms for vortex pairing, dipole ascending and spinning are shown in figure 9. The cause of vortex pairing can be attributed to the velocities induced by the secondary vortices attached to the solid wall. The secondary vortices can induce a downstream (or upstream) velocity on the positive (or negative) vortex cores. As a result, the positive and negative vortex cores tend to approach each other and form pairs (dipoles). The ascending of dipoles is caused by the mutual induction of the two vortices within each vortex pair. The cause of the anticlockwise spinning of the dipoles can be attributed to the fact that the positive vortex is always stronger than the negative one within each pair. The reason why the positive and negative vortices shed into the wake are not equal in strength is still is not fully understood. We conjecture that in the process of vortex formation, the negative vortex cores are closer to the solid wall and thus diffuse more intensively than their positive counterparts.

The phenomenon of vortex pairing (formation of dipoles) due to wall confinement was also reported in inviscid simulations of rigid pitching foil [10] and (passively) fluttering flexible plate [21]. Interestingly, in *inviscid* simulations, the induced velocities on the vortex cores are caused by the *images* vortices, which are analogous to the secondary vortices observed in current viscous simulations. In studying the wall effect on the propulsion of a rigid pitching foil, the spinning of dipoles was also observed in experiments [10]. However, in that study, the vortex dipoles were found to spin in the *clockwise* direction, which is in contradiction with the result of current work. By comparing the problem settings of these two studies, we think that there are several factors which can affect the strength of the positive and negative vortices, which in turn, causes the reversal of the dipoles' spinning direction. First, the foil is driven by a pitching motion in [10], which is different from the plunging motion considered here. Second, due to a much higher *Re* number in the experiments, the viscous effect in [10] is much smaller than that in current work. Moreover, in the experiments of [10], the pitching foil is placed in a steady stream near a *stationary* wall and thus the vortex shedding process is also interfered by the vorticity generated in a fully developed boundary layer.

Here we also probe into the asymmetric properties of the foil's deformation, power input and force production under the wall effect, which are closely associated with the asymmetric wake structures shown in figure 7. Figure 10 shows the time histories of the trailing-edge's vertical position, (instantaneous) input power and (instantaneous) horizontal and lateral forces, for the foil with moderate bending rigidity ($\gamma = 10$). It is seen that the asymmetric features in the foil's deformation, input power and force production are only noticeable at close wall proximity ($\bar{D} < 0.5$). The asymmetry in the trailing-edge's position shown in figure 10(a) indicates that the downward (passive) motion of the trailing-edge is restricted due to the presence of the solid wall. After

Figure 7. Wake structures (vorticity contours) for foils with various bending rigidities and wall proximities. The blue and red colors denote vortex cores with clockwise and anticlockwise rotations, respectively. The thickened black lines denote the solid walls. For cases of $\bar{D} = 6.0$, the solid walls are too far to be included.

the integration of the instantaneous input power (figure 10(b)), it is found that with extreme wall effect ($\bar{D} = 0.2$), the input power during downstroke ($7T_p \leqslant t \leqslant 7.5T_p$) is roughly 14% larger than that during upstroke ($7.5T_p < t \leqslant 8T_p$).
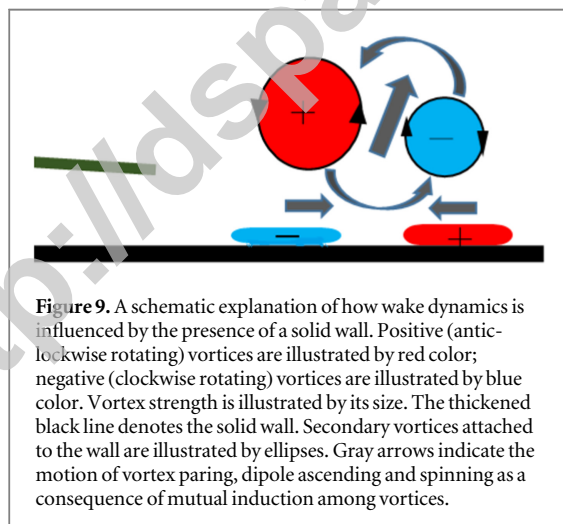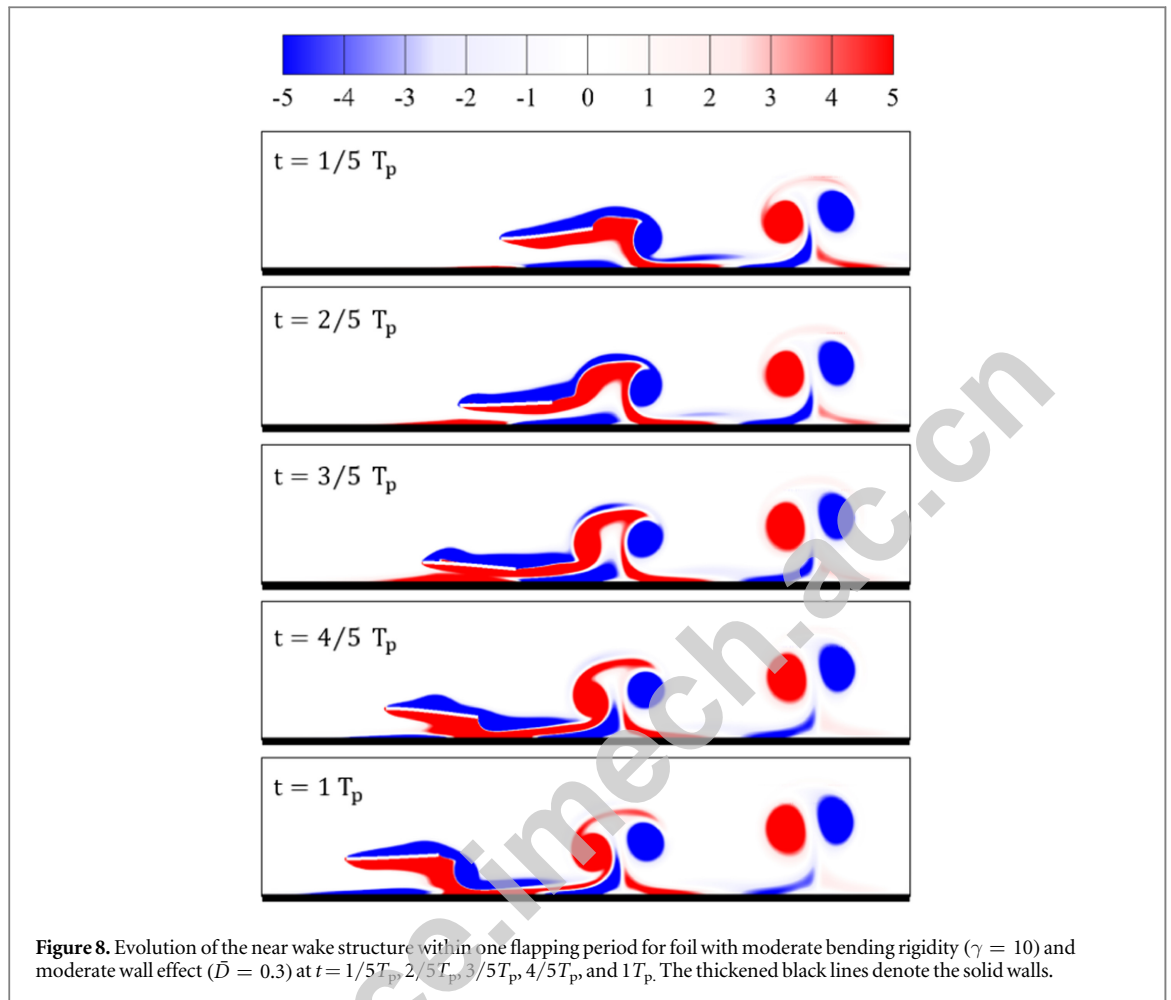
By examining the influence of a solid wall on the proportionality of the streamwise kinetic energy in the flow field, here we propose a preliminary explanation for the enhanced performance in foils with unsteady wall effect. From figure 11, we can see that for a flapper at close wall proximity, a larger proportion of the

kinetic energy is diverted into the propulsion direction (*x*-direction). Presumably, this energy redistribution is favorable for achieving a higher performance.

3.6. Biological implications
Here we investigate the effects of a solid wall on the free-swimming of a simple mechanical flapper. Although this model is non-biological, some biological implications can still be found.
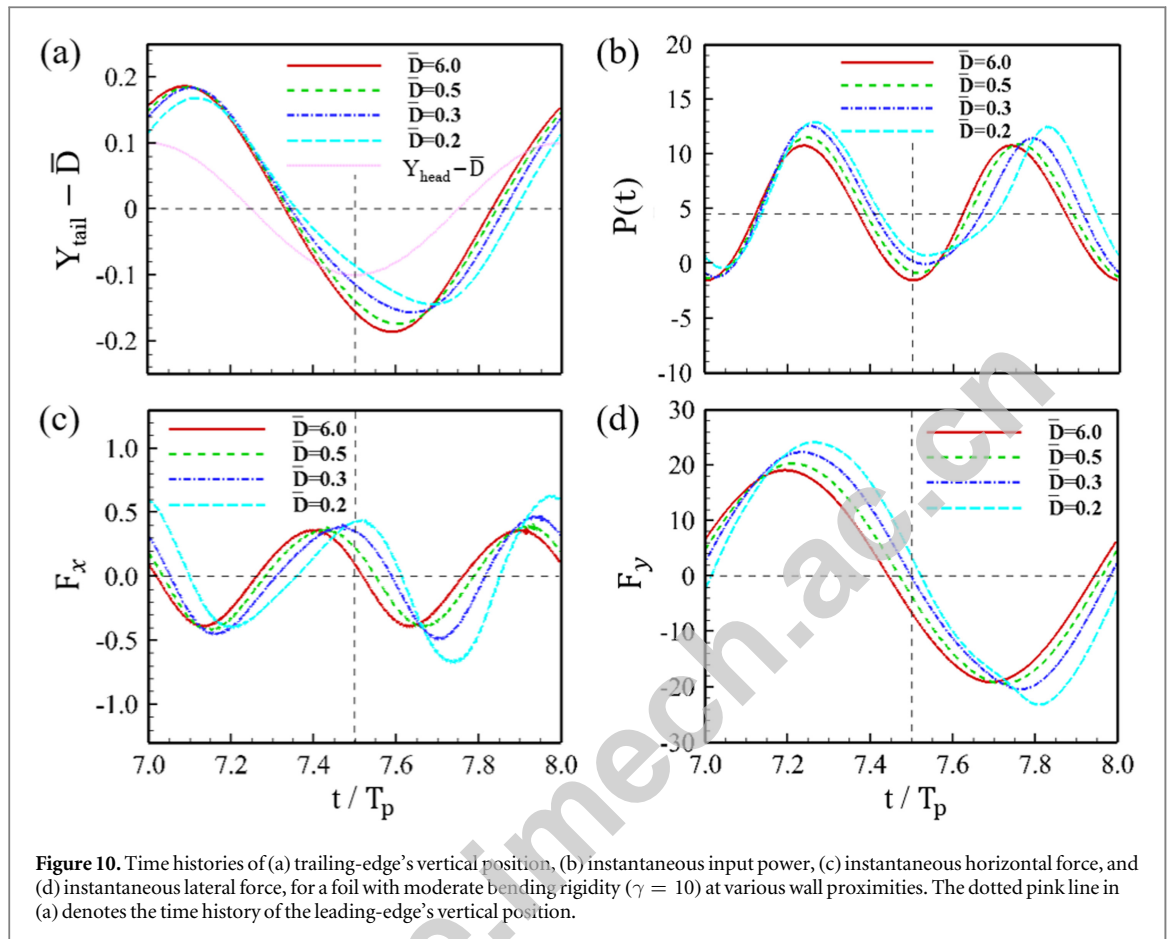
Several key control parameters considered in this work are similar to those in some experimental models

Figure 8. Evolution of the near wake structure within one flapping period for foil with moderate bending rigidity ($\gamma = 10$) and moderate wall effect ($\bar{D} = 0.3$) at $t = 1/5T_p, 2/5T_p, 3/5T_p, 4/5T_p$, and $1T_p$. The thickened black lines denote the solid walls.

Figure 9. A schematic explanation of how wake dynamics is influenced by the presence of a solid wall. Positive (anticlockwise rotating) vortices are illustrated by red color; negative (clockwise rotating) vortices are illustrated by blue color. Vortex strength is illustrated by its size. The thickened black line denotes the solid wall. Secondary vortices attached to the wall are illustrated by ellipses. Gray arrows indicate the motion of vortex paring, dipole ascending and spinning as a consequence of mutual induction among vortices.

or living aquatic animals. The density ratio of 0.03 considered in this work is similar to that measured for eels [22] (which possess body length of 0.2 –0.3 m, body thickness of 0.004 –0.008 m, and body density close to that of water). For a model sunfish studied in [23], the passive body stiffness can vary from the minimum of 10^{-6} (N m^2) near the tail to the maximum of 10^{-3} (N m^2) near the head. The equivalent range for the *dimensionless* bending rigidity is approximately

from 10^{-5} to 1. Thus the lowest bending rigidity considered here are within the range considered in [23]. In the experiment on plaices swimming near the bottom [5], the distances to the substrate varied from 0.04 to 1.0 propulsor span. In the investigation of the effect of solid channel walls on swimming steelhead trout [4], the wall proximities studied were in between 0.11 and 2.71 propulsor span. Thus the range of wall proximity considered in the present study partially overlaps with those of some previous experiments on living fish.

We demonstrate that for a self-propeller flapper, benefits can be gained from the wall effect, such as enhanced cruising speed and/or propulsive efficiency. The results of this work also indicate that rigid flapper are inferior to the flexible ones in near-wall swimming. A rigid flapper may achieve high *percentage* increase in cruising speed, however, the propulsive efficiency can be even reduced due to increasing energetic cost. Please also note that although flexible flappers may gain less *percentage* increase in the cruising speed, their absolute speeds in near-wall swimming can still be higher than that of the rigid flapper. This is because the reference cruising speed (i.e., cruising speed for swimming in an unbounded domain) in flexible flapper can be higher than that in the rigid one (see figure 3). Another disadvantage of the rigid flapper in near-wall

Figure 10. Time histories of (a) trailing-edge's vertical position, (b) instantaneous input power, (c) instantaneous horizontal force, and (d) instantaneous lateral force, for a foil with moderate bending rigidity ($\gamma = 10$) at various wall proximities. The dotted pink line in (a) denotes the time history of the leading-edge's vertical position.

swimming is that the production of averaged lateral force can be quite large. Thus for animals swimming steadily near a surface, more efforts are needed to counteract the averaged lateral force if rigid propulsors are used.

Many aquatic animals moving near boundaries not only use flexible flappers but also actively alter their stiffness during locomotion [11]. The results of the current work shed some light on the importance of flexibility in exploiting the unsteady wall effect for performance improvement. It is also suggested that for near-wall swimming a compromise between the gains in speed and efficiency can be reached by subtly tuning the stiffness of bodies and fins.
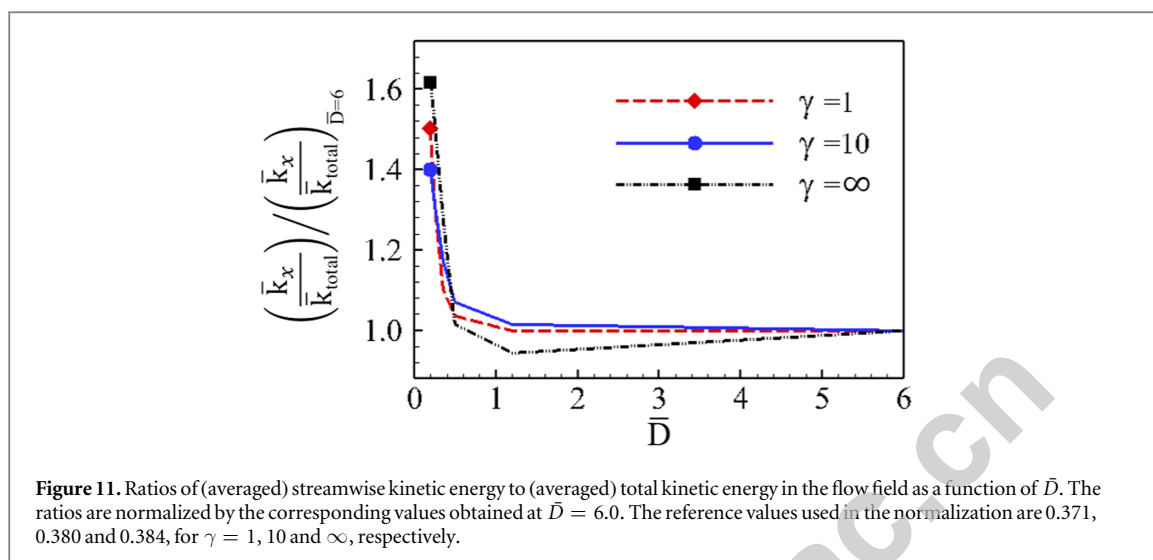
4. Conclusions

The numerical results of this study indicate that the presence of a wall can enhance the cruising speed of a self-propelled plunging foil, with the cost of increasing input power. The rigid foil can achieve high percentage increase in cruising speed but its propulsive efficiency may even decrease. Foils with some passive flexibilities can enjoy a boost in both cruising speed and efficiency. Moreover, when swimming near a wall, flexible foils produce smaller averaged lift forces than the rigid foil.

The introduction of an underneath wall breaks the up–down symmetry of the flow field. The foils' deformation, power input and force production also exhibit some asymmetric features with the presence of a solid wall. Under the influence of wall confinement, the wake structure behind the foil transits from a conventional reversed Karman vortex street into a deflected vortex street consisting of vortex dipoles. The phenomena of vortex pairing, dipole ascending and spinning observed in the wakes with wall effect can be explained by the mutual induction among vortices.

Although the model considered in this work is non-biological, the results obtained here provide some insights into the unsteady wall effect experienced by free-swimming aquatic animals. These results can also be used to inform the design of bio-mimetic underwater vehicles which are capable of making use of the unsteady wall effect.

In the future work, the link between the altered wake structure due to unsteady wall effect and the enhancement in propulsive performance should be carefully studied. The influences of actuating kinematics and Reynolds number on the near-wall swimming of flexible flappers also need to be systematically investigated. Furthermore, optimization of swimming performance by using flappers with varying and actively controlled stiffness along the chord can be another avenue for future research.

Figure 11. Ratios of (averaged) streamwise kinetic energy to (averaged) total kinetic energy in the flow field as a function of $\bar{D}$. The ratios are normalized by the corresponding values obtained at $\bar{D} = 6.0$. The reference values used in the normalization are 0.371, 0.380 and 0.384, for $\gamma = 1$, 10 and ∞, respectively.

Acknowledgments

References

[1] Withers P C and Timko P L 1977 The significance of ground effect to the aerodynamic cost of flight and energetics of the black skimmer (*rhyncops nigra*) *J. Exp. Biol.* **70** 13–26
[2] Hainsworth F R 1988 Induced drag savings from ground effect and formation flight in brown pelicans *J. Exp. Biol.* **135** 431–44
[3] Park H and Choi H 2010 Aerodynamic characteristics of flying fish in gliding flight *J. Exp. Biol.* **213** 3269–79
[4] Webb P W 1993 The effect of solid and porous channel walls on steady swimming of steelhead trout *oncorhynchus mykiss J. Exp. Biol.* **178** 97–108
[5] Webb P W 2002 Kinematics of plaice, *Pleuronectes platessa*, and cod, *Gadus morhua*, swimming near the bottom *J. Exp. Biol.* **205** 2125–34
[6] Blake R W 1983 Mechanics of gliding birds with special reference to the influence of ground effect *J. Biomech.* **16** 649–54
[7] Rayner J M V 1991 On the aerodynamics of animal flight in ground effect *Phil. Trans. Biol. Sci.* **334** 119–28
[8] Tanida Y 2001 Ground effect in fight (birds, fishes and high-speed vehicle) *JSME Int. J.* B **44** 481–6
[9] Iosilevskii G 2008 Asymptotic theory of an oscillating wing section in weak ground effect *Eur. J. Mech.* **27** 477–90
[10] Quinn D B, Moored K W, Dewey P A and Smits A J 2014 Unsteady propulsion near a solid boundary *J. Fluid Mech.* **742** 152–70
[11] Quinn D B, Lauder G V and Smits A J 2014 Flexible propulsors in ground effect *Bioinspir. Biomim.* **9** 1–8
[12] Fernandez-Prats R, Raspa V, Thiria B, Huera-Huarte F and Godoy-Diana R 2015 Large-amplitude undulatory swimming near a wall *Bioinspir. Biomim.* **10** 1–15
[13] Blevins E and Lauder G V 2013 Swimming near the substrate: a simple robotic model of stingray locomotion *Bioinspir. Biomim.* **8** 1–12
[14] Liang H, Wang X J, Zou L and Zong Z 2014 Numerical study of two-dimensional heaving airfoils in ground effect *J. Fluids Struct.* **48** 188–202
[15] Molina J and Zhang X 2011 Aerodynamics of a heaving aerofoil in ground effect *AIAA J.* **49** 1168–79
[16] Moryossef Y and Levy Y 2004 Effect of oscillations on aerofoils in close proximity to the ground *AIAA J.* **42** 1755–64
[17] Wang S Z and Zhang X 2011 An immersed boundary method based on discrete stream function formulation for two- and three-dimensional incompressible flows *J. Comput. Phys.* **230** 3479–99
[18] Huang W X, Shin S J and Sung H J 2007 Simulation of flexible filaments in a uniform flow by the immersed boundary method *J. Comput. Phys.* **226** 2206–28
[19] Zhu X J, He G W and Zhang X 2014 Numerical study on hydrodynamic effect of flexibility in a self-propelled plunging foil *Comput. Fluids* **97** 1–20
[20] Blevins E and Lauder G V 2012 Rajiform locomotion: three-dimensional kinematics of the pectoral fin surface during swimming in the freshwater stingray *Potamotrygon Orbignyi J. Exp. Biol.* **215** 3231–41
[21] Alben S 2015 Flag flutter in inviscid channel flow *Phys. Fluids* **27** 033603
[22] Long J H 1998 Muscles, elastic energy, and the dynamics of body stiffness in swimming eels *Am. Zool.* **38** 771–92
[23] McHenry M J, Pell C A and Long J H Jr 1995 Mechanical control of swimming speed: stiffness and axial wave form in undulating fish models *J. Exp. Biol.* **198** 2293–305